

Optics Letters

Phase-mismatched localized fields in A-PPLN waveguide devices

DEREK CHANG,^{1,2,*} YU-WEI LIN,¹ CARSTEN LANGROCK,¹ C. R. PHILLIPS,^{1,3}
C. V. BENNETT,² AND M. M. FEJER¹

¹E. L. Ginzton Laboratory, Stanford University, Stanford, California 94305, USA

²Lawrence Livermore National Laboratory, Livermore, California 94551, USA

³Department of Physics, Institute of Quantum Electronics, ETH Zurich, Zurich 8093, Switzerland

*Corresponding author: djychang@stanford.edu

Received 19 October 2015; revised 14 December 2015; accepted 16 December 2015; posted 16 December 2015 (Doc. ID 251392); published 13 January 2016

Highly phase-mismatched nonlinear interactions can generate spatially localized optical fields that can affect the performance of nonlinear optical devices. We present a theoretical description of the generation of such spatially localized optical fields by ultrafast pulses. The effects of temporal walk-off and pump depletion are discussed, along with methods for suppression of the localized field while maintaining the performance of the nonlinear device. The model is validated by the measurement of the spatial profile of the localized field in a quasi-phase-matched (QPM) aperiodically poled lithium niobate (A-PPLN) waveguide. Finally, we fabricate and characterize A-PPLN devices with a 33% duty cycle to reduce the locally generated field by 90%. © 2016 Optical Society of America

OCIS codes: (190.4360) Nonlinear optics, devices; (320.7110) Ultrafast nonlinear optics; (190.5330) Photorefractive optics; (190.4975) Parametric processes.

<http://dx.doi.org/10.1364/OL.41.000400>

Lithium niobate (LiNbO₃) is widely used for nonlinear optical frequency conversion [1], and the advent of quasi-phase matching [2,3] has led to a wide range of practical applications [4]. Unfortunately, congruent LiNbO₃ (CLN) suffers from optically induced changes in the refractive index, which causes beam distortion and alters phase matching of nonlinear optical interactions [5]. Photo-refractive damage (PRD) can be reduced by using magnesium-doped LiNbO₃ [6] or by modifying the QPM structure [7]. However, CLN is still advantageous in applications where PRD does not limit the performance [4] due to its more advanced waveguide technologies.

In many applications, both the spectral amplitude and phase imposed by the mixing process, as quantified in the ratio of output field to the appropriate product of input fields, are relevant performance parameters. Distortions in this complex transfer function (CTF) [8] can be caused by PRD-induced changes in the local phase matching, hence compromising device functionality. If the effects of PRD are small and uni-

form along the length of the device, then the phase-matching error is uniform, and the CTF simply shifts in spectrum, leaving the overall profile unchanged. However, if the effects of PRD are not uniform, then phase-matching errors vary spatially and the CTF will exhibit distortions. Such spatially nonuniform changes in phase matching can be generated by spatially localized fields resulting from phase-mismatched interactions in a nonuniform QPM grating.

We begin with a discussion of the generation of localized fields in pulsed interactions, including effects of temporal walk-off and pump depletion. Next, we present measurements of the spatial profile of the local field for various wavelengths and powers in a typical linearly chirped PPLN second-harmonic generation (SHG) device pumped with femtosecond pulses. Finally, we demonstrate how this field can be suppressed via QPM grating design. We focus on the generation and effects of the local fields, rather than the complex topic of PRD [9,10].

The localized field is illustrated by analyzing SHG in a linearly chirped QPM A-PPLN waveguide device. The QPM grating profile is chosen to phase match SHG of the first-harmonic pulse \mathcal{A}_1 . However, with enough power, \mathcal{A}_1 and its second-harmonic, \mathcal{A}_2 , can generate noticeable amounts of third-harmonic \mathcal{A}_3 , despite this process being far from phase matched, i.e., $\Delta k \approx 10^3 \text{ cm}^{-1}$; here, $\Delta k = k_3 - k_2 - k_1$ is the wave vector mismatch. \mathcal{A}_3 is the localized field that can deleteriously affect device performance. The propagation equation for \mathcal{A}_3 is

$$\frac{\partial}{\partial z} \mathcal{A}_3 = -i\kappa_3 \bar{d} \mathcal{A}_1 \mathcal{A}_2 \exp(i\Delta k z), \quad (1)$$

where $\bar{d}(z)$ is the z -dependence of the nonlinear coefficient. The envelope \mathcal{A}_j is related to the electric field E_j by $E_j(x, y, z) = \sqrt{2/n_j \epsilon_0 c} \mathcal{A}_j(z) \mathcal{E}_j(x, y) \exp(-ik_j z)$ for $j \in \{1, 2, 3\}$, where \mathcal{E}_j is the normalized transverse field amplitude. These functions are normalized such that $\iint |\mathcal{E}_j|^2 dx dy = 1$ and $|\mathcal{A}_j|^2$ is equal to the optical power of field j . The coupling coefficient κ_j is defined as $\kappa_j \equiv \theta(8\pi^2 d_0^2 / n_1 n_2 n_3 c \epsilon_0 \lambda_j^2)^{1/2}$, where c is the speed of light, λ_j is the center wavelength of field \mathcal{A}_j , n_j is the index of refraction for the j th wave, $d_0 = \chi^{(2)}/2$ is the amplitude of the pertinent component of the nonlinear susceptibility

tensor, and $\theta = \iint \tilde{d} \mathcal{E}_1 \mathcal{E}_2 \mathcal{E}_3 dx dy$ is the spatial overlap of the interacting modes, where $\tilde{d}(x, y)$ is the transverse spatial distribution of the nonlinear coefficient, but assumed constant in later analysis. We restrict our analysis to the fundamental spatial modes in \mathcal{A}_1 and \mathcal{A}_2 ; our devices were designed to use input/output waveguide tapers to ensure single-mode operation. From simulations of proton diffusion in lithium niobate [11], we computed spatial mode indices and concluded that higher-order spatial modes in \mathcal{A}_3 are negligible as they contribute less than 2% to the total local field.

We consider a nonuniform QPM grating where variations in the local grating period and duty cycle are slow, compared with the grating period itself, such that \tilde{d} can be accurately represented by a sum of distinct Fourier components G_m , with a z -dependent k -vector. The general form of $\tilde{d}(z)$ is

$$\tilde{d}(z) = \sum_m G_m \exp[iK_m z + i\Phi_m(z)], \quad (2)$$

where $G_m = 1/(m\pi) \sin(m\pi\mathcal{D})$ is the amplitude of the m th Fourier component of the grating, and \mathcal{D} is the grating duty cycle. A linear component $K_m = 2\pi m/\Lambda$ is explicitly separated out of the total grating phase, where Λ is the period of the grating, and $\Phi_m(z)$ represents the phase of the grating beyond the K_m component. The average coherence length for generating \mathcal{A}_3 is $\pi/\Delta k_m$, where $\Delta k_m = k_3 - k_2 - k_1 - K_m$. Since the grating is designed to phase match SHG, the corresponding coherence length for generating \mathcal{A}_3 is very short, compared with the length of the device and the distances over which \mathcal{A}_1 and \mathcal{A}_2 amplitudes change significantly, suggesting the use of multiple scales analysis [12] to understand the generation of \mathcal{A}_3 . This analysis leads to

$$\mathcal{A}_3 = \kappa_3 \sum_m \frac{G_m}{\Delta k_m} \mathcal{A}_1 \mathcal{A}_2 \exp(i\varphi_m), \quad (3)$$

where $\varphi_m = \Delta k_m z + \Phi_m$ is the total phase mismatch. Cross-terms from combinations of different grating Fourier components are of the order $\mathcal{O}(1/\Delta k_m^2)$ and are considered to be insignificant. As a result, \mathcal{A}_3 is generated from the sum of contributions from distinct Fourier components of the grating and is proportional to the spatial and temporal overlap of \mathcal{A}_1 and \mathcal{A}_2 .

The time-domain picture of generating \mathcal{A}_3 from SFG in a linearly chirped QPM grating is illustrated in Fig. 1. Pulse \mathcal{A}_1 with bandwidth Ω_0 propagates through the grating with group velocity u_1 . Frequencies in \mathcal{A}_1 phase match to generate second-harmonic frequencies in \mathcal{A}_2 over a phase-match length $L_p = \delta\nu\Omega_0/4D_g$, where D_g is the chirp rate of the grating and $\delta\nu = 1/u_2 - 1/u_1$ is the group velocity mismatch parameter. \mathcal{A}_2 then travels freely with group velocity $u_2 \neq u_1$. While \mathcal{A}_1 and \mathcal{A}_2 overlap in space and time, \mathcal{A}_3 is generated, but once SHG for \mathcal{A}_1 is no longer phase matched, \mathcal{A}_2 is no longer generated, and the overlap between \mathcal{A}_1 and \mathcal{A}_2 decreases as the

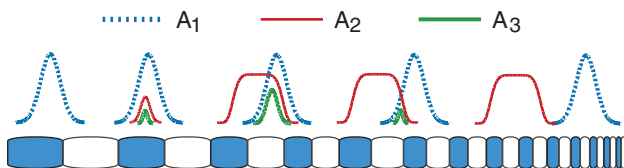


Fig. 1. Time-domain illustration of local field \mathcal{A}_3 generation due to SFG in a chirped QPM grating.

fields walk off each other over a length $L_w = 1/\delta\nu\Omega_0$. \mathcal{A}_3 vanishes once \mathcal{A}_1 and \mathcal{A}_2 no longer overlap and, as a result, it can only exist locally in a finite spatial region of the grating, which we define as w .

If this local field \mathcal{A}_3 causes PRD, then its spatial extent determines the portion of the transfer function that is distorted, and its maximum pulse energy affects the magnitude of the distortion. These factors depend on parameters such as pulse bandwidth Ω_0 , pulse chirp C , and grating chirp D_g .

To understand the relationship between these factors and parameters, we must evaluate Eq. (3). It will be convenient to work in the frequency domain so we define a frequency domain envelope $\hat{A}_j(z, \Omega_j) = \hat{A}_j(z, \Omega_j) \exp\{i[k(\omega_j + \Omega_j) - k(\omega_j)]z\}$, where $\hat{A}_j(z, \Omega_j)$ is the Fourier transform of $A_j(z, t)$ and $\Omega_j = \omega - \omega_j$ is the angular frequency detuning from carrier frequency ω_j . For simplicity, we assume \hat{A}_1 is undepleted and that there is negligible GVD so that $\hat{A}_1(z, \Omega_1) = \hat{A}_1(0, \Omega_1)$ and, thus, write \hat{A}_2 in terms of the fundamental \hat{A}_1 via the transfer function $\hat{D}(z, \Omega_2)$ [13], according to $\hat{A}_2(z, \Omega_2) = \hat{D}(z, \Omega_2) \hat{A}_1^2(\Omega_2)$, where $\hat{A}_1^2(\Omega_2)$ is the convolution $\hat{A}_1(\Omega_1) \otimes \hat{A}_1(\Omega_1)$. With these representations for the fields, Eq. (3) becomes

$$\hat{A}_3^{(m)}(z, \Omega_3) = \kappa_3 \frac{G_m}{\Delta k_m} \{ \hat{D}(z, \Omega_2) [\hat{A}_1(\Omega_1) \otimes \hat{A}_1(\Omega_1)] \otimes \hat{A}_1(\Omega_1) \exp[i\varphi_m(z)]. \quad (4)$$

To compute \hat{A}_3 and illustrate the basic properties of local fields, we consider a linearly chirped pulse \hat{A}_1 with chirp rate $C = C_1\Omega_0^2$ and bandwidth Ω_0 propagating through a linearly chirped grating with chirp rate D_g as defined in [13]. To simplify the analysis, we only consider the first Fourier component, $m = 1$, and assume an infinitely long grating in which $\tilde{d}(x, y)$ is constant. By computing \hat{A}_3 , we can calculate the spatial extent w and maximum pulse energy U of the localized field.

In Fig. 2, we explore how the normalized length $\tilde{w} = w/L\sqrt{D_g L/(1/L)}$ varies with normalized bandwidth $\tilde{\Omega}_0 = \delta\nu\Omega_0/\sqrt{4D_g} = \sqrt{L_p/L_w}$ for different chirp C . The length \tilde{w} represents the fraction of the grating, of length L , where \hat{A}_3

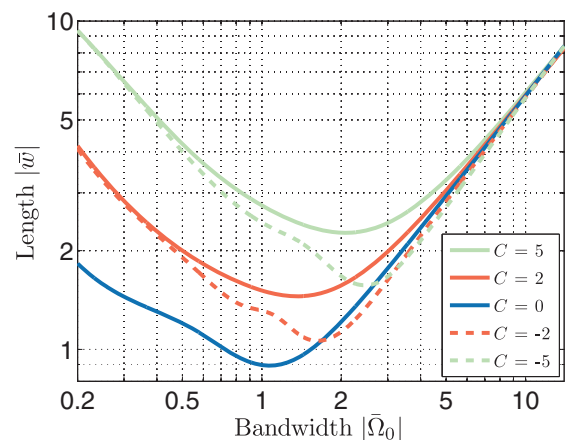


Fig. 2. Length \tilde{w} of locally generated field \hat{A}_3 varies with pulse bandwidth $\tilde{\Omega}_0$ for different chirp C , where $D_g > 0$ is assumed.

exists, scaled by the square root of the ratio of the chirped grating bandwidth, $D_g L$, to the uniform grating bandwidth $1/L$. \tilde{w} grows with increased phase-match length L_p or walk-off length L_w . First, consider \hat{A}_1 to be a transform-limited pulse ($C = 0$). For small bandwidths ($L_w \gg L_p$), \hat{A}_1 is broad in time which increases the walk-off length and results in increased \tilde{w} . For large bandwidths ($L_p \gg L_w$), \hat{A}_1 phase matches over a longer length which also increases \tilde{w} . However, for bandwidths near unity ($L_p \approx L_w$), neither effect dominates, and \tilde{w} is at its minimum.

Now consider a chirped pulse ($C \neq 0$). For larger chirp rates $|C|$, \hat{A}_1 is broader in time which increases the walk-off length and results in increased \tilde{w} . The curves shift toward larger lengths, and the minimum shifts toward larger bandwidths. Pulses with chirp C , such that $C/D_g < 0$, have a chirp that partially cancels out the grating chirp and temporally compresses \hat{A}_2 . This decreases the walk-off length L_w and, therefore, \tilde{w} is smaller compared with those generated by pulses with $C/D_g > 0$.

In Fig. 3, we explore how the normalized pulse energy $\tilde{U} = U/[\kappa_2^2 \kappa_3^2 G_m^2 U_0^3 / (2D_g \Delta k_1^2)]$ of \hat{A}_3 depends on $\tilde{\Omega}_0$. The normalization factor represents the energy in the third-harmonic generated by a CW first-harmonic with power equal to that of a flat-top pulse of energy U_0 and duration $1/\Omega_0$, where U_0 is the pulse energy of \hat{A}_1 . For small bandwidths ($L_w \gg L_p$), \hat{A}_1 is broad in time and, therefore, the peak power is less, which means \hat{A}_3 will have lower power \tilde{U} . For large bandwidths ($L_p \gg L_w$), \hat{A}_1 is compressed, and its peak power increases, resulting in higher \tilde{U} . For larger chirp rates $|C|$, \hat{A}_1 is broader and \tilde{U} decreases. Pulses with chirp C , such that $C/D_g < 0$, generate a temporally compressed \hat{A}_2 and, therefore, increase \tilde{U} .

To the extent that a localized field is causing PRD, it is important to choose parameters so that $\tilde{w} > \sqrt{D_g L / (1/L)}$; as a result, $w > L$ and, therefore, the CTF only shifts in spectrum. Additionally, it is advantageous to choose a smaller bandwidth $\tilde{\Omega}_0$ so that the pulse energy is minimized.

The position of the local field within the grating can change due to changes in the center wavelength or depletion level of \hat{A}_1 . This effect is potentially important as it can alter the spatial

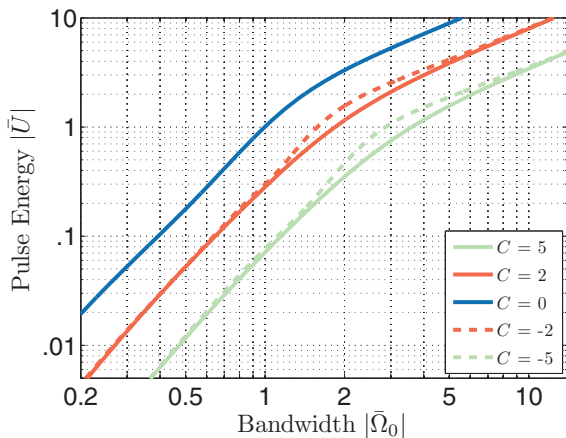


Fig. 3. Maximum pulse energy \tilde{U} of locally generated field \hat{A}_3 varies with pulse bandwidth $\tilde{\Omega}_0$ for different chirp C , where $D_g > 0$ is assumed.

profile of the localized field. We explore these effects experimentally in an A-PPLN waveguide device by measuring the spatial profile of the locally generated field, \hat{A}_3 , by collecting light scattered out of the waveguide at the chip surface along the length of the waveguide. A 400 μm core fiber, oriented at 45° with respect to surface normal, is scanned along the waveguide, and the collected light is detected with a silicon avalanche photodiode; a bandpass filter ensures that only \hat{A}_3 is detected. We assume the scattered light measured at any given position is proportional to $|\hat{A}_3|^2$.

Our A-PPLN device has a QPM grating length of 43 mm and a bandwidth of 22 nm, centered at 1560 nm with a grating chirp rate of $D_g = 0.07 \text{ mm}^{-2}$. The sign of the chirp is such that shorter wavelengths phase match later in the grating. Our transform-limited input \hat{A}_1 has a bandwidth of 16 nm, which is equivalent to $\Omega_0 = 7.4$; we therefore expect $\tilde{w} = 4.7$, i.e., $w = 18 \text{ mm}$ based on Fig. 2. We launch 2.5 mW of \hat{A}_1 into the waveguide and measure the local field profile for $\lambda_1 = 1550 \text{ nm}$, 1560 nm, and 1570 nm, shown as the blue lines in Figs. 4(a)–4(c). Theoretical plots, obtained via numerical simulations of Eq. (1) and the corresponding equations for the evolution of \mathcal{A}_1 and \mathcal{A}_2 to enable inclusion of pump-depletion effects, are shown as the red lines. The peak position shifts toward the end of the grating as λ_1 becomes shorter, and the length matches the expected value of 20 mm, as shown in Fig. 4(b). In Figs. 4(d)–4(f), we fix the center wavelength at 1550 nm and change the input power of \hat{A}_1 for each scan (2.5 mW, 10 mW, and 20 mW). As the power is increased, \hat{A}_1 depletes as a larger fraction is converted to \hat{A}_2 . As a result, the product $\hat{A}_1 \hat{A}_2$ decays along the waveguide, and the peak position shifts closer to the beginning of the grating.

Distortions in the CTF due to local-field-induced PRD can be minimized by reducing the local field intensity through lowering the input power of \hat{A}_1 at the expense of reduced efficiency of the main interaction. Another way is to increase the operating temperature of the device such that the space charge field can be screened more effectively by increased electron mobility [14]; however, excessive temperatures can change waveguide

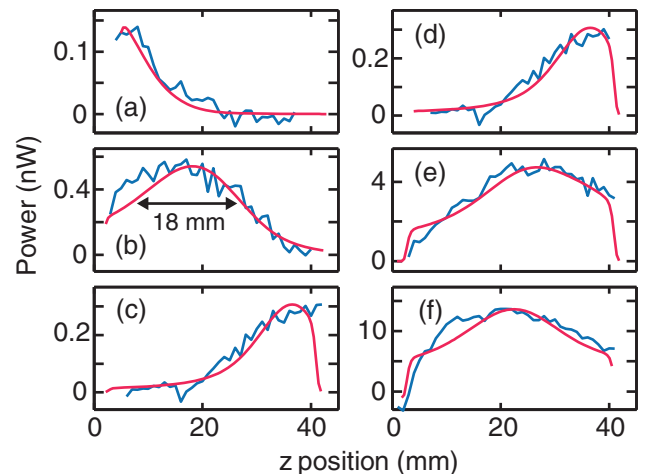


Fig. 4. Measurement (blue) and simulation (red) of local field spatial profile using input power of 2.5 mW with center wavelengths at (a) 1570 nm, (b) 1560 nm, and (c) 1550 nm, and using center wavelength at 1550 nm with input powers of (d) 2.5 mW, (e) 10 mW, and (f) 20 mW.

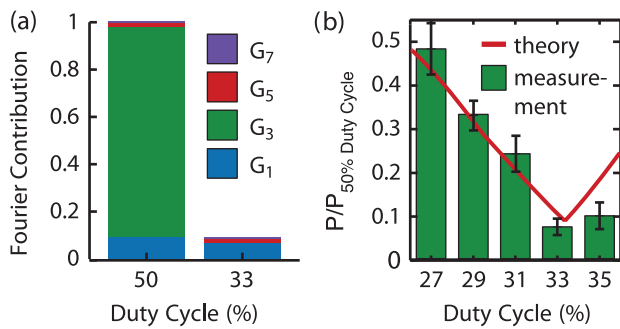


Fig. 5. (a) QPM Fourier component contribution to local field power for 50% and 33% duty cycles. (b) Fabricated 33% duty cycle gratings suppress the local field power by an average of 90%, compared with standard 50% duty cycle grating.

properties. It is also possible to consult Fig. 2 and design the length of the local field to span the entire length of the grating such that transfer function distortion is uniform, and the overall effect is a constant frequency shift, though these designs may not be consistent with the requirements for a given application. Therefore, it is often advantageous to design the QPM grating to minimize local field generation. This can be achieved by adjusting the grating duty cycle \mathcal{D} . The locally generated field, \hat{A}_3 , is composed of contributions from different orders of the QPM grating as seen in Eq. (3). Each contribution is weighted by the factor $G_m/\Delta k_m$. In Fig. 5(a), we illustrate the contribution of each grating order to the total local field for a grating with 50% duty cycle. The third-order Fourier component G_3 provides the largest contribution, but can be eliminated by setting $\mathcal{D} = 33\%$. The ratio of $|\hat{A}_3|^2$ for 33% to 50% duty cycles is about 13%; by setting $\mathcal{D} = 33\%$, $|\hat{A}_3|^2$ can be reduced by almost 90%. The trade-off is a 14% reduction in SHG efficiency due to the reduction of the first-order Fourier component G_1 .

To demonstrate this effect, we test devices with 33% duty cycle QPM gratings. We measured the amount of \hat{A}_3 generated by scanning a tunable, CW laser at 1550 nm across the bandwidth of our devices and measured $|\hat{A}_3|^2$ with a lock-in detection scheme. Figure 5(b) illustrates the amount of \hat{A}_3 generated for different gratings with duty cycles bracketed around 33% as a percentage of the amount of \hat{A}_3 generated for a 50% duty cycle grating. The values are averages over different gratings of identical design. The minimum amount of \hat{A}_3 generated is

about 8%, and the measured results follow the theoretical trend. The slight discrepancy at larger duty cycles can be attributed to measurement inaccuracy as the amount of \hat{A}_3 is quite small. With this design, the local field power is suppressed by almost 10 dB, and one can expect much improved device performance.

In summary, we have provided a model for understanding a general class of parasitic effects called localized fields in A-PPLN waveguide devices. This theory is supported by strong agreement between simulation and measurement results. To improve device performance, we have demonstrated that the average power of localized fields can be suppressed by 10 dB by using a 33% duty cycle grating. The analysis and design presented offers guidance for designing optical frequency converters that avoid the effects of localized fields.

Funding. Air Force Office of Scientific Research (AFOSR) (FA9550-12-1-0110); U.S. Department of Energy (DOE) (DE-AC52-07NA27344).

REFERENCES

1. R. S. Weis and T. K. Gaylord, *Appl. Phys. A* **37**, 191 (1985).
2. M. M. Fejer, G. A. Magel, D. H. Jundt, and R. L. Byer, *IEEE J. Quantum Electron.* **28**, 2631 (1992).
3. J. A. Armstrong, N. Bloembergen, J. Ducuing, and P. S. Pershan, *Phys. Rev.* **127**, 1918 (1962).
4. C. Langrock, S. Kumar, J. E. McGeehan, A. E. Willner, and M. M. Fejer, *J. Lightwave Technol.* **24**, 2579 (2006).
5. A. M. Glass, *Opt. Eng.* **17**, 175470 (1978).
6. D. A. Bryan, R. Gerson, and H. E. Tomaschke, *Appl. Phys. Lett.* **44**, 847 (1984).
7. H. H. Lim, S. Kurimura, and N. E. Yu, *Opt. Express* **22**, 5209 (2014).
8. D. Chang, C. Langrock, Y.-W. Lin, C. R. Phillips, C. V. Bennett, and M. M. Fejer, *Opt. Lett.* **39**, 5106 (2014).
9. M. Carrascosa, J. Villarroel, J. Carnicero, and J. M. Cabrera, *Opt. Express* **16**, 115 (2008).
10. J. Villarroel, J. Carnicero, F. Luedtke, M. Carrascosa, A. García-Cabañes, J. M. Cabrera, A. Alcazar, and B. Ramiro, *Opt. Express* **18**, 20852 (2010).
11. R. V. Roussev, C. Langrock, J. R. Kurz, and M. M. Fejer, *Opt. Lett.* **29**, 1518 (2004).
12. C. Conti, S. Trillo, P. Di Trapani, J. Kilius, A. Bramati, S. Minardi, W. Chinaglia, and G. Valiulis, *J. Opt. Soc. Am. B* **19**, 852 (2002).
13. G. Imeshev, M. A. Arbore, and M. M. Fejer, *J. Opt. Soc. Am. B* **17**, 304 (2000).
14. G. D. Miller, R. G. Batchko, W. M. Tulloch, D. R. Weise, M. M. Fejer, and R. L. Byer, *Opt. Lett.* **22**, 1834 (1997).